Response of the Indian Ocean Basin Mode and Its Capacitor Effect to Global Warming*

XIAO-TONG ZHENG

Physical Oceanography Laboratory, Ocean–Atmosphere Interaction and Climate Laboratory, Ocean University of China, Qingdao, China

SHANG-PING XIE

International Pacific Research Center, and Department of Meteorology, School of Ocean and Earth Science and Technology, University of Hawaii at Manoa, Honolulu, Hawaii, and Physical Oceanography Laboratory, Ocean–Atmosphere Interaction and Climate Laboratory, Ocean University of China, Qingdao, China

QINYU LIU

Physical Oceanography Laboratory, Ocean–Atmosphere Interaction and Climate Laboratory, Ocean University of China, Qingdao, China

(Manuscript received 26 October 2010, in final form 6 May 2011)

ABSTRACT

The development of the Indian Ocean basin (IOB) mode and its change under global warming are investigated using a pair of integrations with the Geophysical Fluid Dynamics Laboratory Climate Model version 2.1 (CM2.1). In the simulation under constant climate forcing, the El Niño–induced warming over the tropical Indian Ocean (TIO) and its capacitor effect on summer northwest Pacific climate are reproduced realistically. In the simulation forced by increased greenhouse gas concentrations, the IOB mode and its summer capacitor effect are enhanced in persistence following El Niño, even though the ENSO itself weakens in response to global warming. In the prior spring, an antisymmetric pattern of rainfall–wind anomalies and the meridional SST gradient across the equator strengthen via increased wind–evaporation–sea surface temperature (WES) feedback. ENSO decays slightly faster in global warming. During the summer following El Niño decay, the resultant decrease in equatorial Pacific SST strengthens the SST contrast with the enhanced TIO warming, increasing the sea level pressure gradient and intensifying the anomalous anticyclone over the northwest Pacific. The easterly wind anomalies associated with the northwest Pacific anticyclone in turn sustain the SST warming over the north Indian Ocean and South China Sea. Thus, the increased TIO capacitor effect is due to enhanced air–sea interaction over the TIO and with the western Pacific. The implications for the observed intensification of the IOB mode and its capacitor effect after the 1970s are discussed.

1. Introduction

El Niño–Southern Oscillation (ENSO) is the first mode of ocean–atmospheric interaction in the equatorial Pacific. ENSO not only dominates in the tropical Pacific region but also influences the climate of other regions. As a remote impact of El Niño, positive anomalies of sea surface temperature develop over the tropical Indian Ocean (TIO) during the winter of the developing year of El Niño, reach the peak in the following spring (Klein et al. 1999; Alexander et al. 2002; Lau and Nath 2003; Schott et al. 2009), and persist through boreal summer (Du et al. 2009). This basinwide warming phenomenon emerges as the first empirical orthogonal function of Indian Ocean SST both in observations and model simulations (Saji et al. 2006; Du et al. 2009; Deser et al. 2010) and is referred to as the Indian Ocean basin (IOB) mode in Yang et al. (2007). Yang et al. (2007) and Li et al.

* International Pacific Research Center Publication Number 797.

Corresponding author address: Xiao-Tong Zheng, College of Physical and Environmental Oceanography, Ocean University of China, Qingdao 266100, China.
E-mail: zhengxt@ouc.edu.cn

DOI: 10.1175/2011JCLI4169.1

(2008) suggest that this prolonged basinwide warming is not simply a passive response to El Niño, but influences climate like a capacitor in the summer when El Niño has dissipated. Specifically the IOB mode anchors an anomalous anticyclone over the northwest Pacific (NWP) via atmospheric Kelvin waves and increases mei-yu–baiu rainfall over East Asia in boreal summer (Xie et al. 2009). In a coupled forecast model, the IOB mode accounts for about 50% of atmospheric anomalies over NWP during June–August [JJA(1)] (Chowdary et al. 2011a) [numerals in the parentheses denote the ENSO developing (0) and decay (1) years]. Furthermore, the TIO warming also suppresses NWP tropical cyclones in the summer following El Niño (Du et al. 2011).

There are numerous studies that investigate mechanisms for the IOB mode formation. Klein et al. (1999) show that much of the IOB mode is caused by ENSO-induced surface heat flux anomalies, including the wind-induced latent heat flux and solar radiation flux due to suppressed atmospheric convection over the TIO. Furthermore, a tropospheric temperature (TT) mechanism is proposed to explain the formation of the IOB mode (Chiang and Sobel 2002; Chiang and Lintner 2005): Because of the increased tropospheric temperature over the tropics during El Niño (Yulaeva and Wallace 1994), the temperature and humidity of the atmospheric boundary layer over deep convection regions rise, thereby increasing the SST via turbulent heat flux. In the tropical southwest IO (SWIO) however, the warming cannot be explained by surface fluxes (Klein et al. 1999), for which ocean dynamics are important (Xie et al. 2002; Huang and Kinter 2002). In the developing and mature phases of El Niño, there are anticyclonic wind anomalies over the southern TIO, which force a downwelling Rossby wave (Masumoto and Meyers 1998). The Rossby wave propagates westward to the SWIO where the mean thermocline is shallow, deepens the thermocline, and raises SST (Xie et al. 2002).

Recent studies suggest that the IOB mode is not uniform in space but shows spatial variations. A series of TIO–atmosphere interactions helps the IOB mode persist through the summer and shapes its spatiotemporal structures. In boreal spring, the SWIO warming induces an antisymmetric pattern of atmospheric anomalies. There is more (less) rainfall than normal, with northwesterly (northeasterly) wind anomalies south (north) of the equator (Kawamura et al. 2001; Xie et al. 2002; Wu et al. 2008). Wind–evaporation–sea surface temperature (WES) (Xie and Philander 1994) feedback helps sustain this antisymmetric mode operating on the easterly climatological winds during winter and early spring (Kawamura et al. 2001; Wu et al. 2008). The antisymmetric pattern persists through early summer. When the southwest monsoon begins in May over the north Indian Ocean (NIO), the northeasterly anomalies there act to warm the ocean, inducing a second warming over the NIO and extending the IOB mode through JJA(1) following El Niño (Du et al. 2009). This prolonged IOB mode affects the subtropical NWP and East Asian climate. The schematic in Xie et al. (2010b, Fig. 1) illustrates the air–sea interactions and the capacitor effect.

The IOB mode and its capacitor effect show an interdecadal change around the climate regime shift of the 1970s in observations and atmospheric general circulation model (GCM) studies (Xie et al. 2010b; Huang et al. 2010). After the mid-1970s, the IOB mode strengthens and persists through JJA(1). Most of the aforementioned air–sea interaction processes over TIO are more pronounced after the 1970s, including the ENSO-induced downwelling Rossby wave, the SWIO warming, the antisymmetric wind pattern, the second warming over NIO, and the anticyclonic anomalies over the subtropical NWP. Xie et al. (2010b) suggests that the intensification of ENSO and the thermocline shoaling over the SWIO thermocline ridge lead to this interdecadal change.

Is the increase of IOB mode after the mid-1970s a result of the ongoing global warming due to anthropogenic forcing? It is difficult to answer this question. First, changes in interannual variability of tropical Pacific SST during global warming have been investigated extensively (Meehl et al. 1993; Knutson et al. 1997; Timmermann et al. 1999; Fedorov and Philander 2000; Collins 2005; van Oldenborgh et al. 2005; Capotondi et al. 2006; An et al. 2008; Collins et al. 2010) and appear to vary among models (Guilyardi et al. 2009). Second, observations are too short to determine a long-term trend in ENSO change (Wittenberg 2009). Unlike observations for the past few decades (Xie et al. 2010b; Han et al. 2010), the thermocline deepens over the SWIO in many models because of the weakened Walker circulation during global warming (Zheng et al. 2010), potentially decreasing the local thermocline feedback and weakening the effect of ocean dynamics on SST.

Several studies investigate the response of the Indian Ocean dipole (IOD) mode—the second mode of Indian Ocean SST—to global warming (Abram et al. 2008; Cai et al. 2009; Zheng et al. 2010). The shoaling thermocline in the eastern equatorial Indian Ocean due to a weakened Walker circulation under global warming (Vecchi et al. 2006; Du and Xie 2008) has been proposed as the cause of the increased IOD activity in recent decades (Abram et al. 2008). Based on ocean–atmospheric coupled model simulations, Zheng et al. (2010) suggest that the IOD variance does not change much in global warming because the increased thermocline feedback is

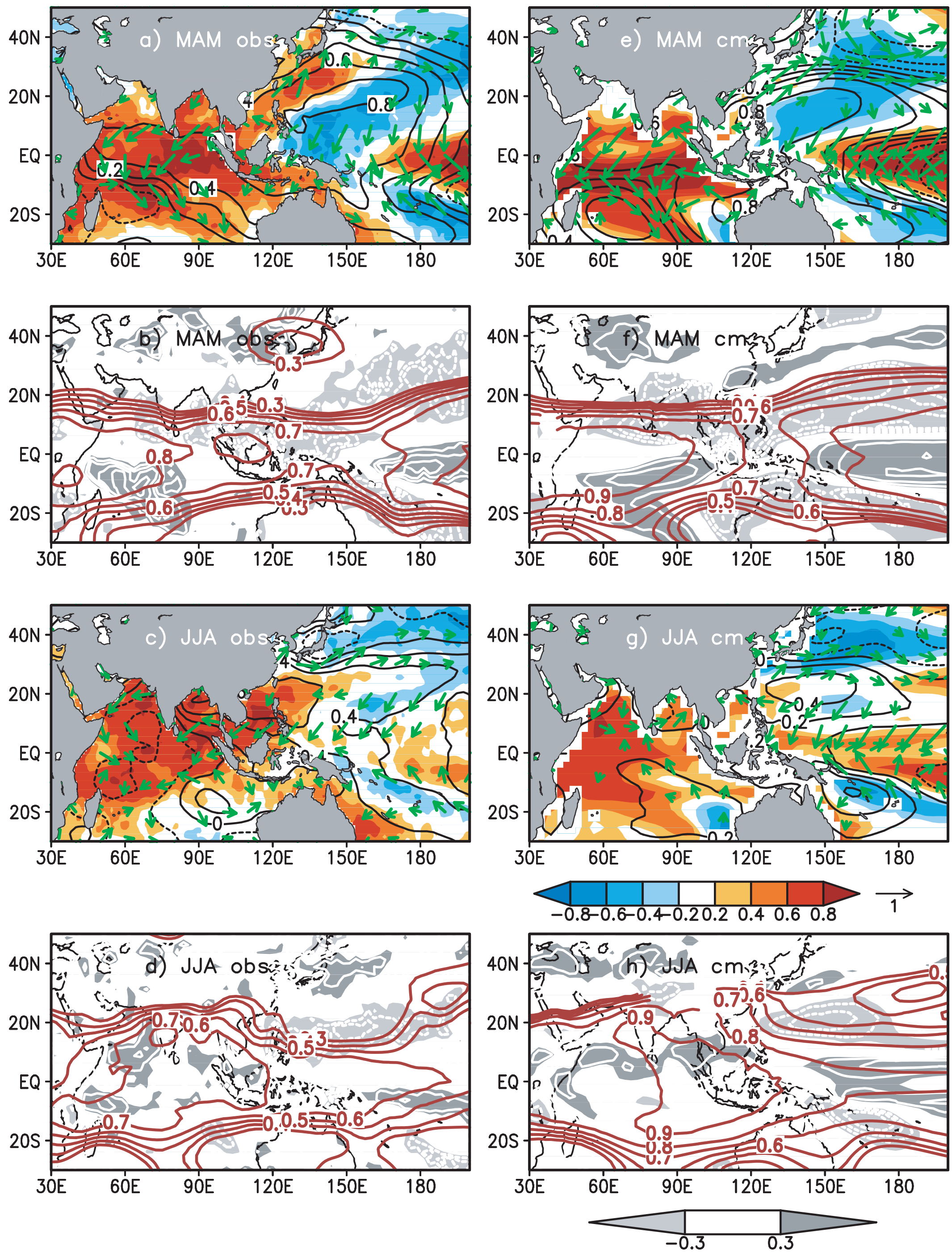

FIG. 1. Correlation with the NDJ(0) ENSO index of observed SST (color), SLP (contours), and surface wind velocity (vectors) during (a) MAM(1) and (c) JJA(1). (b),(d) As in (a),(c) but for tropospheric temperature (contour) and rainfall (gray shade > 0.4 and white contours at intervals of 0.1) in observations. The right-hand panels are for the GFDL CM2.1 control run.

offset by a decreased atmospheric wind feedback. The response to global warming of the first mode of Indian Ocean SST (IOB mode) has not been systematically investigated.

The present study investigates changes in the IOB mode and its capacitor effect under global warming by using a state-of-the-art coupled GCM that simulates the IOB mode very well. Our results show that the IOB mode strengthens in summer during global warming, consistent with observations (Xie et al. 2010b). The enhanced air–sea interactions in the Indo–western Pacific are responsible for the prolonged IOB mode in a warmer climate. As a result, the IOB mode capacitor effect on East Asian climate is more persistent in time under global warming.

The rest of the paper is organized as follows: Section 2 describes the model and simulations. Section 3 analyzes the control run and evaluates the simulation of IOB mode in the coupled model. Section 4 investigates changes in the IOB mode and its air–sea interactions in global warming. Section 5 is a summary.

2. Model and simulations

We use the outputs from the Geophysical Fluid Dynamics Laboratory Climate Model versions 2.1 (GFDL CM2.1), a global, coupled ocean–atmosphere–land–ice model, to study the IOB mode response to global warming. The model formulation and simulation are documented in Delworth et al. (2006). The atmospheric component of the coupled model is the GFDL atmospheric model version 2.1 (AM2.1) (GFDL Global Atmospheric Model Development Team 2004). The model uses a finite volume dynamical core (Lin 2004) with $2.5° \times 2°$ horizontal resolution and 24 vertical layers. The oceanic component is based on the Modular Ocean Model (MOM4) code (Griffies et al. 2003), which has a horizontal resolution of $1° \times 1°$ and 50 vertical layers. In the meridional direction the resolution increases toward the Equator to ⅓° between 30°S and 30°N.

This study analyzes the following two simulations: a 500-yr-long run under constant radiative forcing in 1860 (see Table 1 of Delworth et al. 2006) is used to examine the skill of GFDL CM2.1 in simulating the IOB mode, its air–sea interactions, and capacitor effect. Then we investigate the IOB mode response to global warming by using a 300-yr-long "global warming" run, which is made up of two sections, both from the World Climate Research Program (WCRP) Third Coupled Model Intercomparison Project (CMIP3). One is the last 100 years of the twentieth-century run (20C3M) forced by historical climate forcing from 1861 to 2000. Another is the first 200 years of the 300-yr projection under the Special Report on Emissions Scenarios A1B with a 720-ppm CO_2 stabilization. Since the initial conditions for the A1B experiment are taken from 1 January 2001 of the 20C3M experiment, we combine the two sections to form a 300-yr-long dataset from 1901–2200 to examine the IOB mode response to global warming. The most pronounced warming period is from 2001–2100 in response to the rapid GHG increase. The twentieth and twenty-second centuries represent the current and warmer climate epoch, respectively.

This study focuses on changes in interannual variability of ocean and atmosphere. We perform a three-month running average to reduce intraseasonal variability and calculate a 9-yr running mean to remove decadal and longer variations, which are significant over the tropical Indian Ocean (Deser et al. 2004) in the control and global warming runs. We use SST averaged over the eastern equatorial Pacific (Niño-3.4: 5°S–5°N, 120°–170°W) to track ENSO, which is referred to as the ENSO index.

Saji et al. (2006) shows that many coupled models cannot simulate ENSO teleconnections in the Indian Ocean very well. Only 8 of the 17 CMIP3 CGCMs examined in their study simulate the basinwide SST warming following El Niño. CM2.1 simulates the climatology and leading modes of interannual SST variability over the TIO (Song et al. 2007; Zheng et al. 2010). To examine the model dependence of our analyses, we choose another five models that can simulate the TIO basin warming following El Niño, including GFDL CM2.0 (Delworth et al. 2006), Centre National de Recherches Météorologiques Coupled Global Climate Model, version 3 (CNRM-CM3) (Salas-Mélia et al. 2005), Meteorological Research Institute Coupled General Circulation Model, version 2.3.2 (MRI CGCM2.3.2) (Yukimoto et al. 2001), Met Office (UKMO) third climate configuration of the Met Office Unified Model (HADCM3) (Gordon et al. 2000) and UKMO Hadley Centre Global Environmental Model version 1 (HADGEM1) (Johns et al. 2006).

We use the Hadley Centre Global Sea Surface Temperature (HadSST) dataset (Rayner et al. 2006), the National Centers for Environmental Prediction (NCEP)–National Center for Atmospheric Research (NCAR) atmospheric reanalysis (Kalnay et al. 1996), and the Center for Climate Prediction (CPC) Merged Analysis of Precipitation (CMAP) (Xie and Arkin 1996) from 1979 to 2008 (limited by CMAP) to assess the CM2.1 skill in the IOB mode simulation.

3. IOB mode simulation in the control run

To evaluate the skill of GFDL CM2.1 in reproducing the IOB mode, we first examine the delayed, basinwide warming response over the TIO a few months after ENSO peaks in the Pacific. Compared with observations (left panel, Fig. 1), the spatial distributions of SST, sea level pressure (SLP), precipitation and tropospheric temperature correlation with ENSO in spring and summer in the model (right panel, Fig. 1) show realistic spatiotemporal characteristics of IOB mode. During

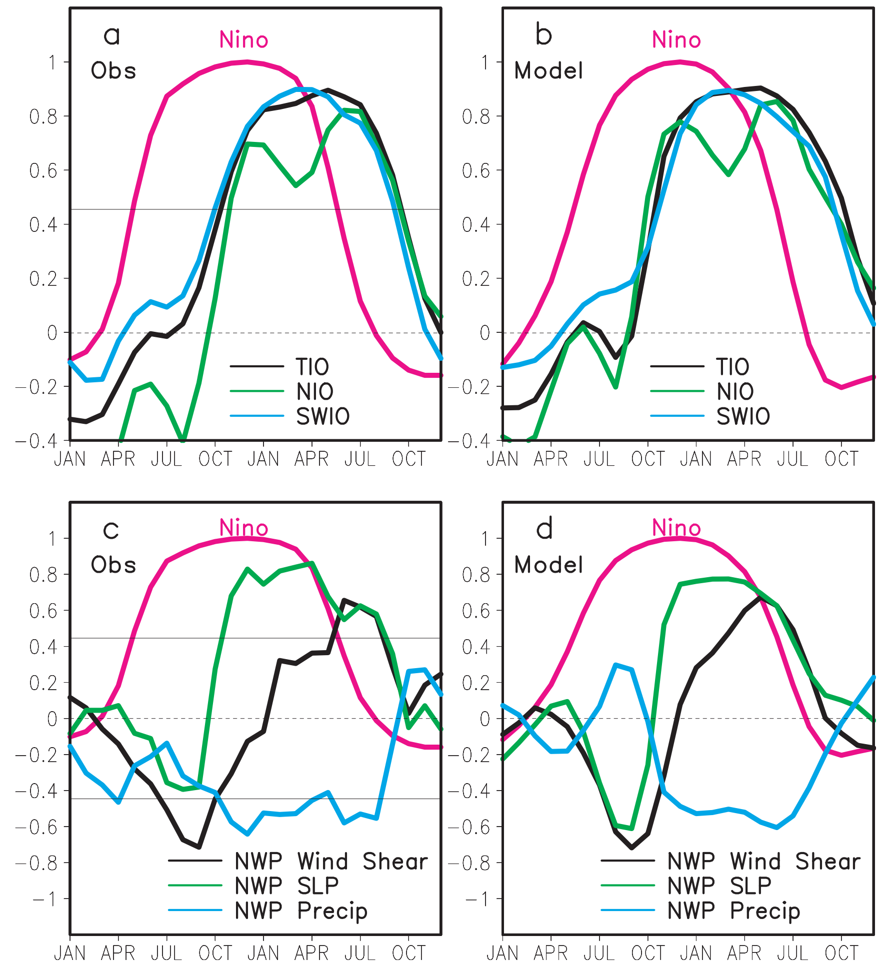

FIG. 2. Correlation with the NDJ(0) ENSO index: (a) SST over the TIO and its subbasins and (c) subtropical NWP SLP, rainfall, and surface wind vorticity defined as (27°–33°N) minus (11°–15°N) zonal wind difference averaged in 120°–160°E during the ENSO developing and decay years in the 1979–2006: (b),(d) for 500-yr unforced model run. The red line is for the lagged autocorrelation of the ENSO index with its NDJ(0) values.

March–May [MAM(1)], the warming is visible in the southern TIO (Figs. 1a,e), which is due to ocean dynamics (Xie et al. 2002; Du et al. 2009) and heat flux exchange (Wu et al. 2008; Wu and Yeh 2010). Both in observations and the model (Figs. 1a,e), the antisymmetric wind (rainfall) pattern appears over the TIO with anomalous northeasterlies (decreased rainfall) north of the equator and northwesterlies (increased rainfall) to the south, accompanied with a cross-equatorial SST gradient. The tropical tropospheric temperature anomalies are zonally uniform in both observations and model during MAM(1) when El Niño signal begins its rapid decay (Figs. 1b,f). During JJA(1) the NIO and South China Sea warm after the summer monsoon onset, while the antisymmetric pattern decays in the atmosphere (Figs. 1c,g). Tropospheric temperature anomalies show a Matsuno(1966)–Gill(1980) pattern (Figs. 1d,h). The NWP anticyclonic circulation is present from MAM(1) to JJA(1) in surface wind and SLP fields (Figs. 1c,g). In MAM(1) the NWP anticyclone is maintained by local negative SST anomalies (Wang et al. 2003). In JJA(1) the local negative SST anomalies decay, and the remote forcing by the TIO warming becomes the main anchor for the NWP anticyclone (Yang et al. 2007; Xie et al. 2009). Although the model captures the main spatial features of IO SST response to ENSO, there are some biases as follows. The warming over the equatorial Pacific is too strong and shifts westward compared with observation, indicating the bias of simulating ENSO in CM2.1 as is documented in Wittenberg et al. (2006). In summer, the SST warming over the Bay of Bengal and SCS is weaker in the model than observations.

The model also simulates the temporal evolution of IOB mode realistically. Figures 2a and 2b compare the lagged correlation with ENSO of SST averaged over the TIO (40°–100°E, 20°S–20°N) and its subbasins [SWIO (50°–80°E, 15°–5°S) and NIO (40°–100°E, 0°–20°N)] between observations and model. For 500-yr time series, a correlation of 0.14 reaches the 99% significance level based on *t* test. The model TIO warming reaches a broad peak in MAM(1) when Niño-3.4 SST anomalies decay rapidly. TIO SST anomalies persist through JJA(1) and decay in August–September(1), similar to observations (Fig. 2a). The SWIO warming, with an important contribution by ocean dynamics, is maximum in March(1) and decays in June(1). The NIO warming shows a double-peak feature. The first warming appears during the mature phase of El Niño while the second emerges during JJA(1) because of the air–sea interactions within the TIO (Izumo et al. 2008; Du et al. 2009). The NIO warming weakens during MAM(1). This characteristic of NIO warming is similar to observations after the mid-1970s when ENSO is significantly stronger (Fig. 2a). Overall, CM2.1 successfully captures the delayed TIO warming response to El Niño.

In addition to the IOB mode, the model also simulates the atmospheric response to El Niño over the subtropical NWP. Figures 2c and 2d compare the lagged correlation of the anomalous NWP anticyclone with ENSO between observations and model. The anomalous anticyclone emerges when El Niño reaches the peak and persists through the summer. This result holds whether we use a zonal wind-shear index [defined as (27.5°–32.5°N) minus (10°–15°N) difference averaged in 120°–160°E], SLP or precipitation averaged in 12.5°–30°N, 120°–160°E to represent the anticyclone. The time evolution of the NWP anticyclone in the model is similar to that in observations (Fig. 2c), indicating the model skill in simulating the atmospheric response over the subtropical NWP.

Du et al. (2009) show that oceanic downwelling Rossby waves are very important for the IOB mode formation. Previous studies show that the model simulates the SWIO thermocline ridge well (e.g., Fig. 5, Saji et al. 2006). Figure 3 shows longitude–time sections of sea surface height (SSH), SST, and Ekman pumping velocity anomalies in the south TIO, as represented by their correlations with the ENSO index. The thermocline deepens in the eastern south TIO during September(0)–December(0) in response to local Ekman downwelling associated with an anomalous anticyclone in the southeast TIO (Xie et al. 2002; Yu et al. 2005; Rao and Behera 2005). SST anomalies over the south TIO peak following the mature phase of ENSO and persist through September (1). The SST copropagation with SSH is not as clear as in observations, as Saji et al. (2006) noted. Downwelling Ekman pumping velocity decays in spring, replaced by an upwelling Ekman pumping signal in the SWIO in response to the SST warming and enhanced atmospheric convection (Annamalai et al. 2005a). Compared with observations (see Fig. 11, Xie et al. 2002), the model simulates the SWIO warming and related ocean dynamics realistically, although the zonal extents of SST and SSH signals are too wide. This discrepancy seems to be associated with a too wide simulated thermoline ridge (see Fig. 5, Saji et al. 2006) and downwelling Ekman pumping (Fig. 3c) in the model.

Figures 4a and 4b compare zonal-mean anomalies of SST and surface wind in time–latitude sections between observations and model. The wind pattern is symmetric during the mature phase of El Niño and easterly on the equator. From March(1) onward, the wind pattern becomes antisymmetric about the equator and the pattern persists through June(1). The antisymmetric pattern is associated with local WES feedback and the SWIO warming in spring (Kawamura et al. 2001; Wu et al. 2008; Du et al. 2009) and eventually causes the second peak in NIO warming after the Indian summer monsoon onset by weakening the mean wind and reducing surface latent heat flux (Du et al. 2009). This NIO warming in summer excites a warm Kelvin wave in tropospheric temperature (Fig. 4d) through August(1) that propagates into the Pacific with a distinctive equatorial peak. The warm tropospheric Kelvin wave anchors the anticyclone in the NWP (Xie et al. 2009). All zonal-mean responses to El Niño are similar to observations, which are shown in Figs. 4a and 4c.

Our analyses show that CM2.1 captures the IOB mode, key air–sea interactions that sustain the mode, and the capacitor effect on NWP. Encouraged by the favorable comparison with observations, we proceed to study the response of IOB mode to global warming.

4. IOB mode response to global warming

The tropical Indian Ocean SST has been steadily increasing over the recent 60 years (Alory et al. 2007; Du and Xie 2008). Meanwhile, interannual warming of the TIO following El Niño has become more persistent after the climate regime shift of the 1970s (Xie et al. 2010b). Interdecadal changes are found in air–sea interaction processes important for the IOB mode, including the SIO downwelling Rossby wave, the antisymmetric wind pattern, the second warming of the NIO, and the anomalous NWP anticyclone. It is still unclear, however, if such interdecadal changes are due to the ongoing global warming. In global warming simulations of CM2.1, the IOB mode shows a similar extended persistence, as in

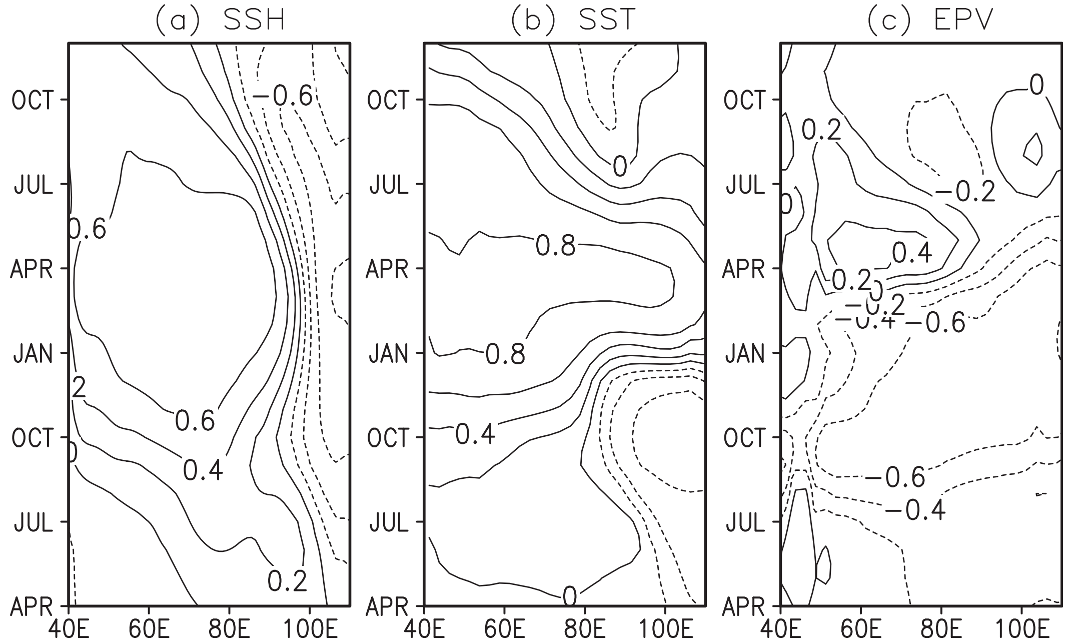

FIG. 3. Correlation with the NDJ(0) ENSO index of (a) SSH, (b) SST, and (c) Ekman pumping velocity averaged from 8° to 12°S for the unforced run.

observations. Figure 5 compares the evolution of the NIO and SCS SST anomalies during a typical El Niño event before and after global warming in the model. The NIO warming during boreal spring is weaker in the twenty-second than the twentieth century. The second warming in boreal summer, by contrast, is more pronounced and persistent in the Bay of Bengal and the SCS. We applied a significance test for the difference in regressions between the twenty-second and twentieth centuries by using the Fisher z transformation (Dunn and Clark 1969). In Fig. 5c, the difference between two epochs is significant over the Bay of Bengal and SCS in summer. The rest of this section examines changes in the IOB mode and its air–sea interactions in response to global warming.

a. Mean state change

Development of the IOB mode and its air–sea interactions depend on the mean state of the TIO (Xie et al. 2010b). First, we examine the mean state change during global warming. Figure 6 shows the change in the TIO and NWP climatology between the twenty-second and twentieth centuries for spring (MAM) and summer (JJA). During MAM, the SST warming shows a nearly uniform pattern over the TIO except for a relatively large warming in the northwestern IO. Surface wind changes show a weakened northeast monsoon in the NIO and enhanced easterly trades in the SWIO. Rainfall changes are small over the TIO and positive in the tropical western Pacific.

In JJA, SST warming over the TIO shows a dipole pattern in the east–west direction along the equator, rising to 3.5°C in the northwestern equatorial IO, but only 2.4°C off the Sumatra coast. As a response to this warming pattern, there is a dipole pattern of rainfall change in the equatorial IO, positive over the northwest TIO and negative over the southeast. This SST–rainfall relationship is consistent with the result of Xie et al. (2010a) that the SST change relative to tropical mean warming determines the distribution of tropical rainfall change (Johnson and Xie 2010). Surface wind change is consistent with those of SST and rainfall—easterly over the equatorial IO and westerly over the equatorial Pacific. The wind change is associated with the weakened Walker circulation under global warming (Held and Soden 2006; Vecchi et al. 2006). This dipole warming pattern, the easterly wind anomalies, and the thermocline shoaling in the equatorial IO are noted in a number of studies (Vecchi and Soden 2007; Du and Xie 2008; Zheng et al. 2010).

b. Interannual TIO warming

In CM2.1, ENSO activity weakens in global warming. The standard deviation of the November–January [NDJ(0)] Niño-3.4 index is reduced from 1.37°C in the twentieth century to 1.02°C in the twenty-second century (Fig. 7a). Furthermore, a typical ENSO event decays slightly earlier in global warming (Fig. 7b). The IOB mode also shows changes during global warming

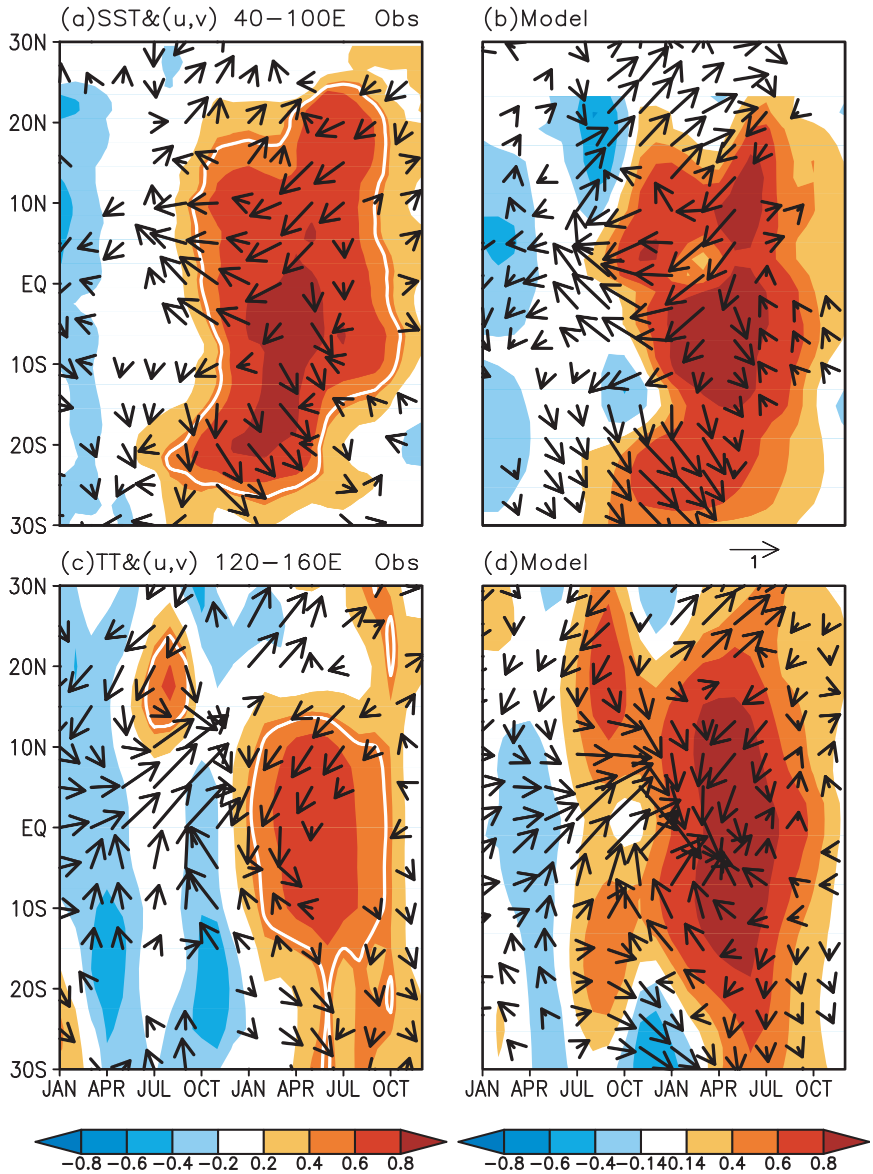

FIG. 4. Correlation with the NDJ(0) ENSO index as a function of calendar month and latitude: (a) surface wind velocity (vectors) and SST (color) over the TIO (40°–100°E zonal mean) and (c) tropospheric temperature (color) and surface wind velocity (vector) averaged over the western Pacific (120°–160°E zonal mean) for 1979–2006. The white contours denote 95% significance level: (b),(d) as in (a),(c) but for 500-yr unforced model run.

(Fig. 5). Figure 8 compares the regression of interannual anomalies of SST and surface wind upon the ENSO index in the twentieth and twenty-second centuries. The overall evolution of the IOB mode from spring to summer is similar before (left panel) and after (middle panel) global warming including the SWIO warming, antisymmetric wind pattern in spring, and second NIO warming in summer. However, there are some noticeable changes in the IOB mode from the twentieth to twenty-second century (right panel, Fig. 8). During MAM(1) in the warmer climate, there is a stronger cross-equatorial SST gradient in the TIO that favors the antisymmetric pattern of surface wind. In summer, the warming over the NIO and SCS strengthens during global warming, and so does the antisymmetric wind pattern in the TIO. Over the NWP the anomalous anticyclone is much stronger after global warming. In June–September [JAS(1)] the post–prewarming change is particularly significant—the anomalous NWP anticyclone is still robust in the twenty-second century but has

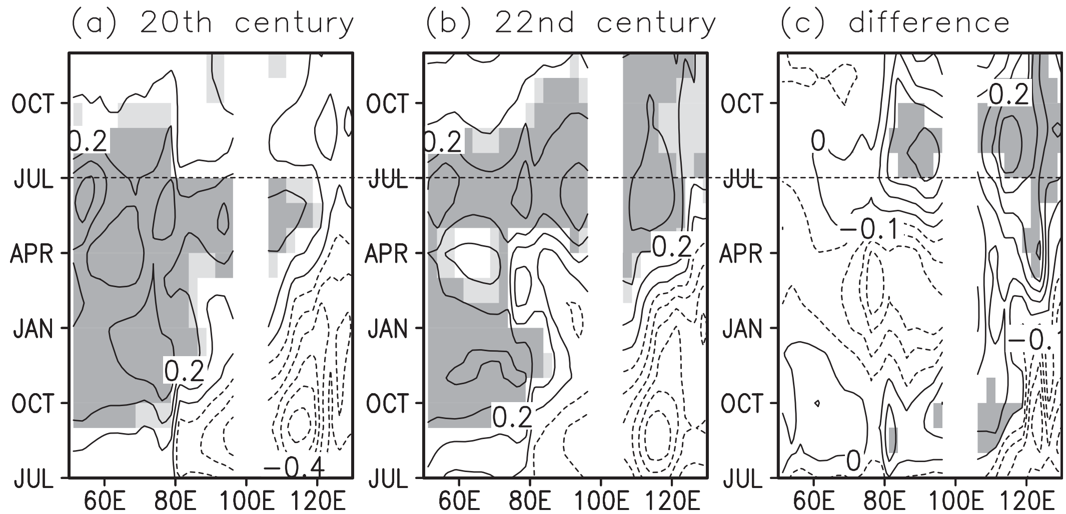

FIG. 5. Regression of SST (°C) average over NIO and SCS (5°–15°N) upon NDJ(0) ENSO index as a function of longitude and calendar month for (a) the twentieth century and (b) twenty-second century and (c) the difference. Values exceeding the 95% (99%) significance level are light (dark) shaded.

decayed almost completely in the twentieth century. All regression changes are above 90% significance level based on the Fisher z transformation.

Despite a decrease in ENSO amplitude, the standard deviation of TIO SST is largely unchanged from the twentieth to twenty-second century because of an increase in their correlation (Fig. 7a). Variance change is an obvious choice to study the IOB mode response to global warming, but the downside is its sensitivity to ENSO amplitude. The response of ENSO amplitude to global warming is highly variable among models and uncertain even with regard to the sign of change (Collins et al. 2010). For this reason this study chooses to examine changes in the regression of TIO/NWP anomalies upon the ENSO index. This is a normalized measure of magnitude change free of uncertainties in ENSO amplitude change. By our regression-based measure, the IOB mode response to ENSO is enhanced and more persistent in global warming, although the ENSO itself weakens. To investigate the IOB mode response to global warming further, next we examine key ocean–atmospheric processes.

c. *Enhanced antisymmetric pattern*

The antisymmetric pattern of the TIO emerges in boreal spring and plays an important role in basinwide warming. We perform an empirical orthogonal function (EOF) analysis of rainfall anomalies during MAM over the tropical Indo–western Pacific (40°–140°E, 30°S–30°N) from 1901 to 2200. The first EOF mode explains about 24% of the total variance. Figure 9 shows the regressions of SST, rainfall, and surface wind anomalies upon the first principal component (PC-1). The spatial distributions are similar to observations (e.g., Fig. 1 in Wu et al. 2008). The time series of this mode is highly correlated with the ENSO index ($r = 0.76$). The SST and

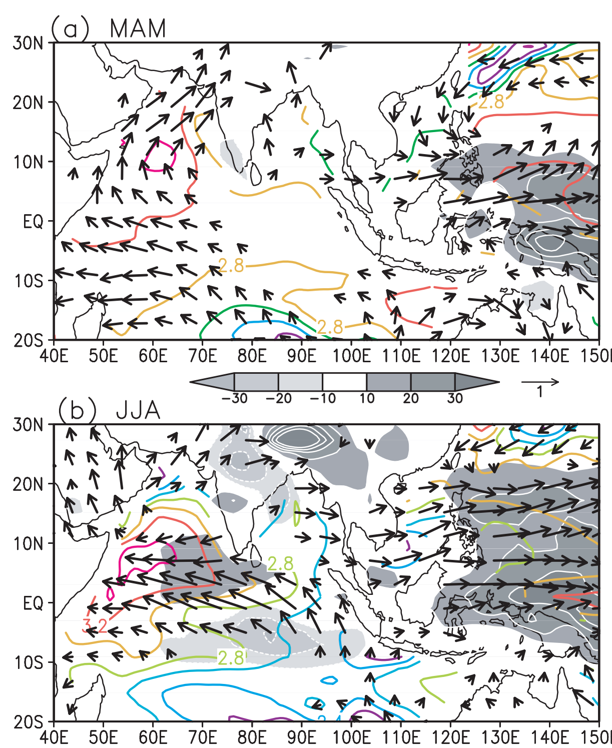

FIG. 6. Twenty-second and twentieth century differences in SST (contours, °C), rainfall (shade, mm month^{-1}), and surface wind velocity (vectors, m s^{-1}) for (a) MAM and (b) JJA.

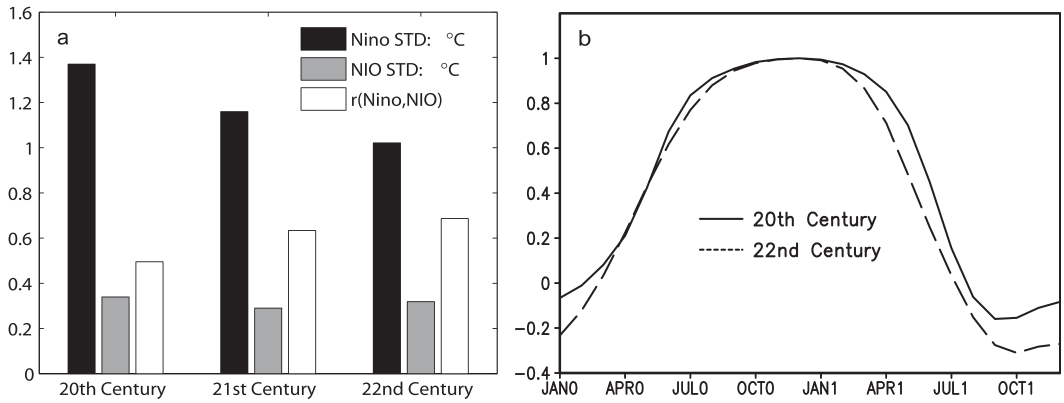

FIG. 7. (a) Standard deviations (°C) of the ENSO index, JAS(1) NIO SST and correlation between them for twentieth, twenty-first, and twenty-second century and (b) lagged autocorrelation of the ENSO index with its NDJ(0) values for the twentieth (Solid line) and twenty-second century (dashed line).

rainfall anomalies show strong north–south contrasts across the equator (Fig. 9a). Positive rainfall anomalies appear in the SWIO in response to the locally enhanced warming, while negative rainfall can be seen in the Bay of Bengal and tropical western Pacific. Surface wind anomalies are consistent with rainfall, northeasterly over the NIO and northwesterly over the SIO. This antisymmetric rainfall/wind pattern is associated with a cross-equatorial gradient in SST anomalies typically found in boreal spring following El Niño (Fig. 9a).

The relationship between the antisymmetric pattern and ENSO is enhanced in a warmer climate in the model. The 51-yr running regression of the normalized PC-1 upon the ENSO index increases from 0.6 to about $0.75\ \mathrm{K}^{-1}$ across 2050 (Fig. 9b, the years denote the centers of sliding windows; for example, 1975 represents the regression in the 51-yr sliding windows of 1950–2000.). Previous studies (Kawamura et al. 2001; Wu et al. 2008) suggest that this antisymmertric pattern of atmospheric anomalies is due to air–sea interactions within the TIO via surface heat fluxes, especially the WES feedback. The intensified antisymmetric pattern suggests an increased importance of WES feedback in global warming. Global warming shoals the ocean mixed layer, which acts to intensify surface feedback such as WES.

We evaluate the WES effect with a latent heat flux decomposition (de Szoeke et al. 2007; Du and Xie 2008; Du et al. 2009). Based on the bulk formula, latent heat flux can be cast as

$$Q_E = \rho_a L C_E W[q_S(T) - \mathrm{RH} q_S(T - \Delta T)], \quad (1)$$

where ρ_a is surface air density, L is the latent heat of evaporation, C_E is the transfer coefficient, W is surface wind speed, $q_S(T)$ is the saturated specific humidity following the Clausius–Clapeyron equation, RH is surface relative humidity, T is SST, and ΔT is difference between the sea and air surface temperature. Latent heat flux can be divided into two parts: atmospheric forcing and oceanic response. The oceanic response can be cast as a Newtonian cooling term $Q'_{\mathrm{EO}} = \alpha \overline{Q_E} T'$, where the overbar and prime denote the mean and perturbation, respectively. The residual $Q'_{\mathrm{EA}} = Q'_E - Q'_{\mathrm{EO}}$ is regarded as atmospheric forcing (WES effect) due mostly to changes in wind speed (W), relative humidity RH, and air–sea temperature difference (ΔT). The WES effect increases over the SWIO during MAM(1) under global warming (Fig. 10, solid line), indicating that enhanced air–sea interaction prolongs the SWIO warming. Over the NIO summer warming is mainly due to the atmospheric (wind speed) forcing via evaporation (Du et al. 2009). In the model, the WES effect in boreal summer is also enhanced for the NIO warming under global warming (Fig. 10, dashed line), strengthening the second warming there. There is variability in the timing of the increase in the WES effect between the SWIO and NIO, likely due to low-frequency natural variability.

Why does the ENSO-induced antisymmetric pattern in the TIO strengthen in global warming? We consider two possible mechanisms. First the WES feedback intensifies in the SIO, as Fig. 10 illustrates. This may be due to the intensification of the mean easterlies in the SIO under global warming (Fig. 6a), which is a necessary condition for WES feedback. Second, we note an increased SST cooling after El Niño in the western equatorial Pacific (right panel of Fig. 8) where the maximum negative rainfall anomalies are located (Fig. 9a). Figure 11 shows the 51-yr running regressions of western Pacific SST and rainfall anomalies on the ENSO index as a function of calendar month and year. Both SST and rainfall display more robust negative anomalies under global warming in boreal spring. This intensification of negative SST

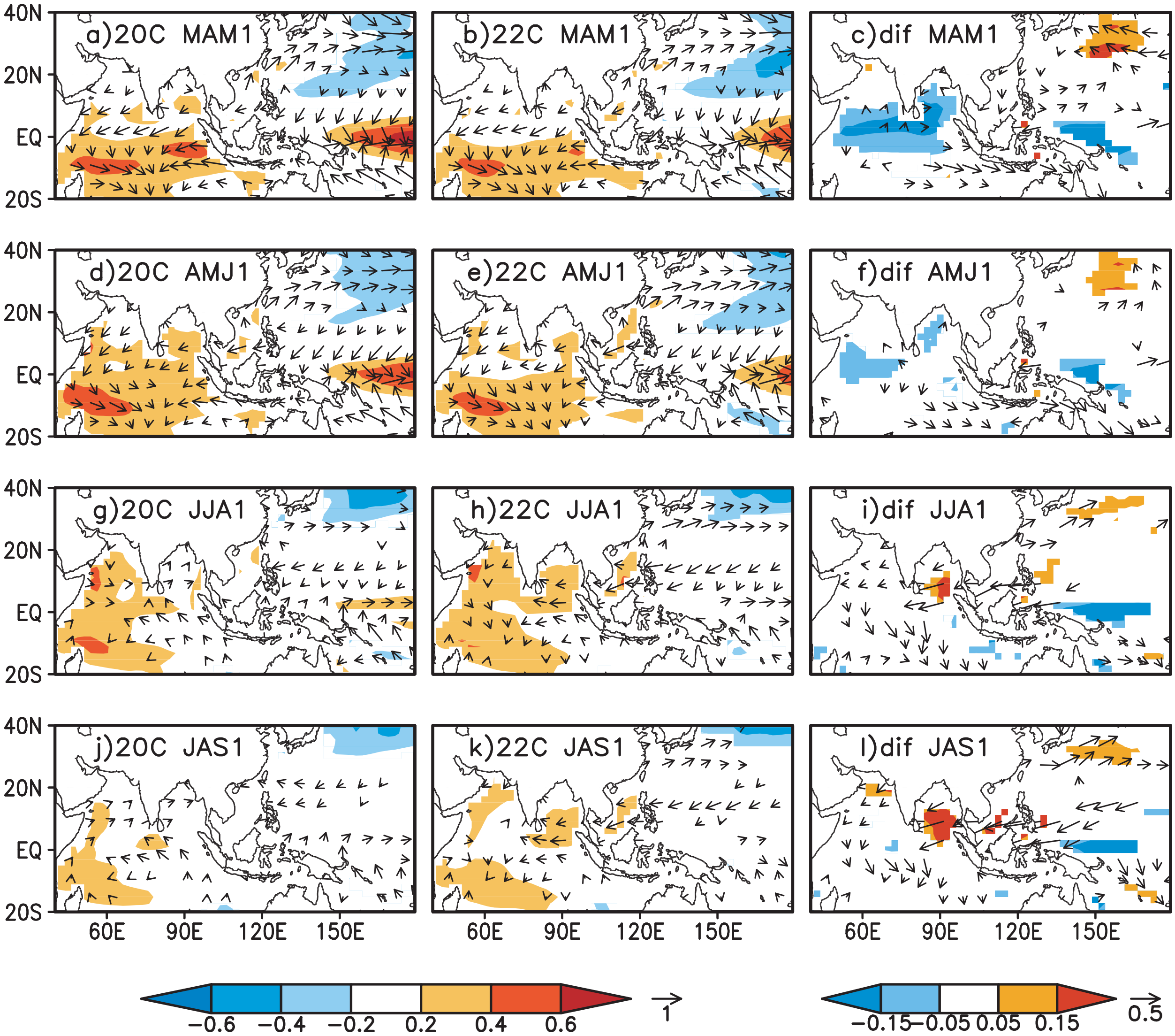

FIG. 8. SST(°C) and surface wind velocity (m s^{-1}) regressed on the NDJ(0) ENSO index during (a)–(c) MAM(1), (d)–(f) April–June [AMJ(1)], (g)–(i) JJA(1), and (j)–(l) JAS(1) for (left) the twentieth century, (middle) twenty-second century, and (right) the twenty-second minus twentieth-century differences. Values exceeding the (left and middle) 95% and (right panels) 90% significance level are shown.

anomalies appears due to the shoaling mean thermocline in response to the weakened Walker circulation in global warming (Vecchi et al. 2006; Vecchi and Soden 2007). If the mean thermocline shoals in the western equatorial Pacific, the interannual tilt of the thermocline during El Niño can impact the local SST more significantly via enhanced thermocline feedback. The effect of surface heat flux tends to damp the negative SST intensification as a response to the enhanced thermocline feedback (not shown). The enhanced SST cooling in the NWP during MAM(1) is found in observations (Huang et al. 2010, Fig. 11) after the 1970s compared to the preclimate regime shift epoch. The antisymmetric wind pattern is closely related with the warming over the SWIO in spring and the NIO in summer following El Niño, which are discussed the next two subsections.

d. Delayed SWIO warming

Figure 12 shows the 51-yr running regression of SWIO SST on the ENSO index as a function of calendar month and year. Although the warming period over the SWIO does not change much, the interannual warming peaks later under global warming. Positive SST anomalies develop at the mature phase of El Niño and peak in April(1) in the current climate. The maximum warming

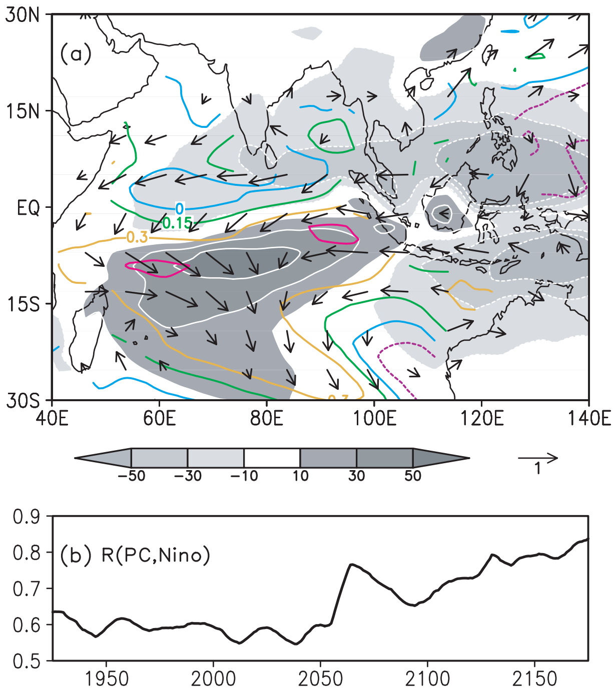

FIG. 9. (a) Regressions of SST (contour, °C), rainfall (gray shade, mm month^{-1}), and surface wind velocity (vectors, m s^{-1}) on the time series of the leading EOF mode for MAM rainfall over the TIO and western Pacific in the global warming run and (b) 51-yr running regression of the time series of leading EOF mode on the NDJ(0) ENSO index.

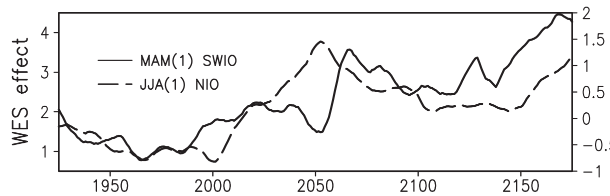

FIG. 10. Fifty-one-year running regression of the atmospheric forcing term (W m^{-2}) over the SWIO (solid line) during MAM(1), and NIO (dashed line) during JJA(1) on the NDJ(0) ENSO index.

appears in June(1) after global warming, a delay of about two months. As part of the antisymmetric wind pattern, westerly wind anomalies during April(1) to June(1) strengthen in the warmer climate, reducing turbulent heat flux by weakening the prevailing southeasterly winds as an enhanced WES effect in Fig. 10.

The SWIO warming is related to the ENSO-induced oceanic dynamic Rossby wave and is important for the IOB mode, and especially for the antisymmetric wind pattern (Du et al. 2009). Figure 13 compares longitude–time sections of changes in SSH, SST, and Ekman pumping velocity anomalies between the twenty-second and twentieth centuries, as represented by their regressions upon the ENSO index. The Ekman pumping velocity during July(0) to November(0) decreases (Fig. 13c), indicative of a reduced teleconnection by ENSO due in part to enhanced atmospheric stability (Zheng et al. 2010). The weakened ENSO activity may also decrease the response of SSH to ENSO since ENSO is just one of many factors such as the IOD, a coupling relation with ENSO that weakens under global warming (Zheng et al. 2010). This change of atmospheric forcing leads to weakened SSH anomalies in the ENSO decay year (Fig. 13a).

In response to an easterly change in the mean wind on the equator (Fig. 6), the mean thermocline deepens in the SWIO (Zheng et al. 2010), reducing the thermocline feedback. As a result, the change of SST anomalies is negative from January(1) to April(1) due to the weakened SSH anomalies and reduced thermocline feedback, but turn positive in boreal summer due to the enhanced antisymmetric pattern and WES feedback (Fig. 13b). This causes a delay in the peak warming over the SWIO after global warming, as Fig. 12 illustrates. Furthermore, the local atmospheric response to SWIO warming appears to increase during global warming, with an enhanced local Ekman pumping velocity (Fig. 13c) over the SWIO in June(1) to October(1).

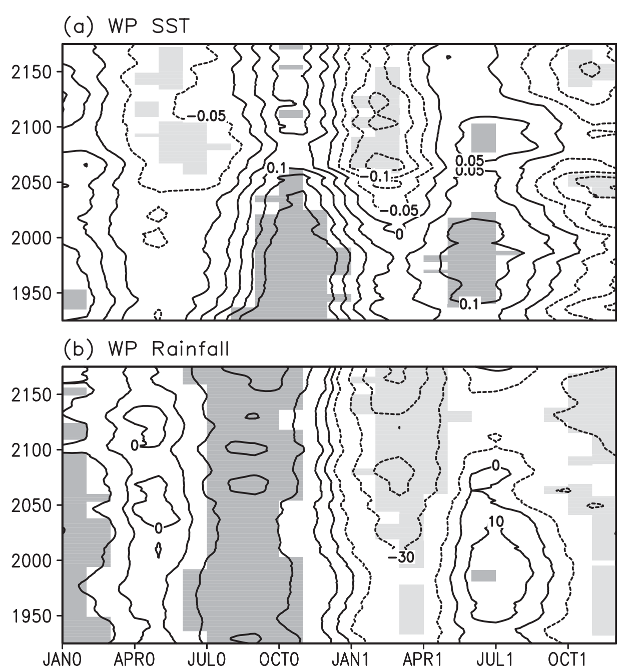

FIG. 11. Fifty-one-year running regression on the NDJ(0) Niño-3.4 SST index as a function of calendar month and year for the developing and decay years of ENSO: (a) SST (°C) and (b) rainfall (mm month^{-1}) in global warming simulation over the western Pacific (averaged in 120°–150°E, 5°S–5°N) and northwestern Pacific (averaged in 120°–150°E, 0°–10°N), respectively. Values exceeding the 95% significance level are shaded.

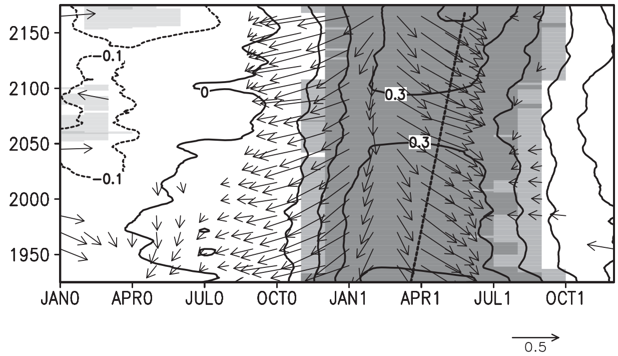

FIG. 12. As in Fig. 11 but for the ENSO index: SST (contours, °C) and surface wind velocity (vectors, m s^{-1}, exceeding 95% significance level) over the SWIO (50°–80°E, 5°-15°S) in global warming simulation. Values exceeding the 95% (99%) significance level are light (dark) shaded.

e. Enhanced persistence in the NIO warming and capacitor effect

The antisymmetric rainfall/wind pattern over the TIO is important for the second warming over the NIO during boreal summer. Specifically, when the summer monsoon starts in May/June (1), the northeasterly anomalies act to reduce the prevailing southwesterlies and warm the ocean, generating the second warming over the NIO and SCS. As the antisymmetric pattern is enhanced in the global warming simulation, the second NIO warming persists much longer. Figure 14 shows the 51-yr running regression of NIO and SCS SST on the ENSO index a function of calendar month and year. The first warming of NIO in winter decreases under global warming due to the weakened ENSO teleconnection associated with enhanced atmospheric stability. The enhanced antisymmetric pattern also weakens the NIO warming in spring by increasing the anomalous easterlies in January(1)–February(1) when the mean wind is easterly. The second warming of NIO peaks in June(1) before the global warming, and shows a tendency for a longer persistence from the twentieth to twenty-second century. The interannual warming exceeding 95% significance terminates in August(1) in the current climate but extends to October(1) in global warming. The increase in easterly wind anomalies is consistent with the enhanced persistence of the second NIO warming. The anomalous easterlies cease in June(1) in the twentieth century but lasts until October(1) in the twenty-second century. As a result, the atmospheric forcing term by latent heat flux increases during JJA(1) in global warming (Fig. 10) to prolong the second NIO warming.

In summer, the easterly anomalies over the NIO and SCS are part of the NWP anticyclone. The NWP anomalous anticyclone persists longer by 1–2 months in global warming, through JAS(1) in the twenty-second century (Fig. 15) despite faster decay in ENSO itself (Fig. 7b).

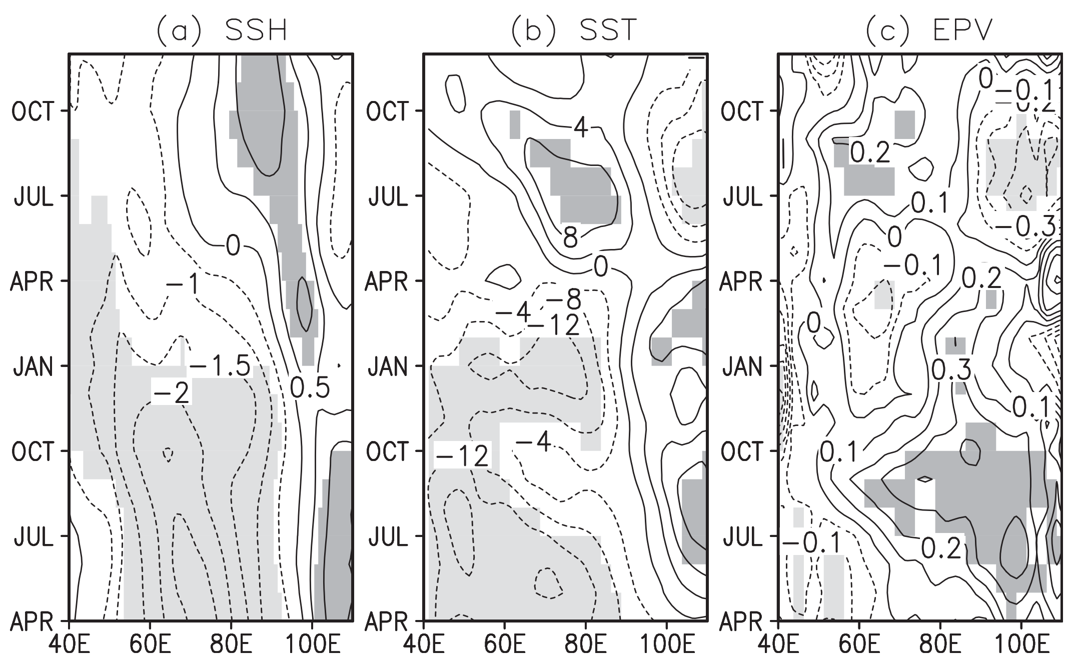

FIG. 13. The twenty-second minus twentieth century differences of regressions on the NDJ(0) ENSO index of (a) SSH (cm), (b) SST (10^{-2} °C), and (c) Ekman pumping velocity (10^{-6} m s^{-1}) averaged from 8° to 12°S. Values exceeding the 90% significance level are shaded.

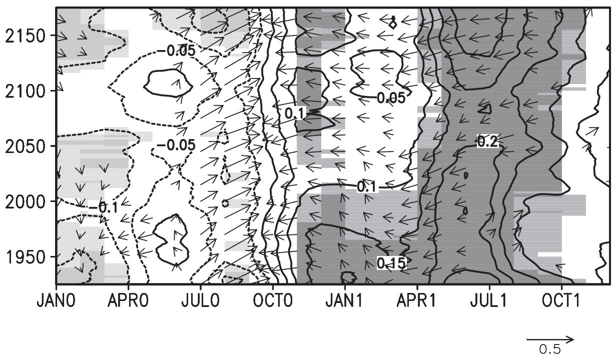

FIG. 14. Fifty-one-year running regression on the NDJ(0) ENSO index as a function of calendar month and year for the developing and decay years of ENSO: SST (contours, °C) and surface wind velocity (vectors, m s^{-1}, exceeding 95% significance level) over the NIO and SCS (averaged in 40°–120°E, 0°–20°N) in the global warming simulation. Values exceeding the 95% (99%) significance level are light (dark) shaded.

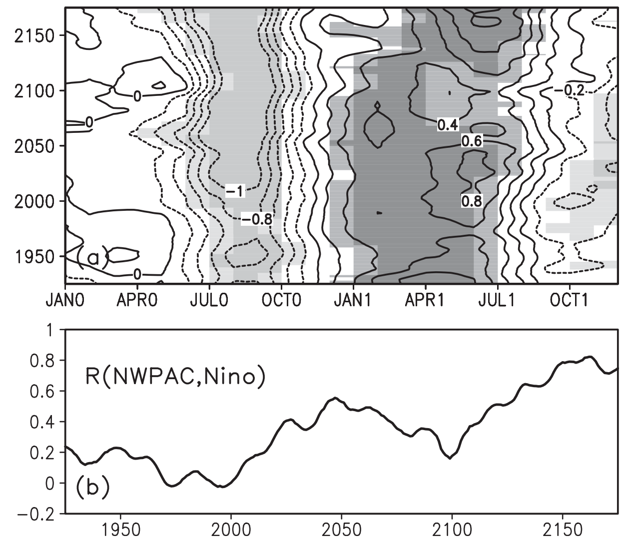

FIG. 15. (a) As in Fig. 14 but Fifty-one-year running regression on the NDJ(0) Niño-3.4 SST index: surface wind vorticity (m s^{-1}) define as (27°–33°N) minus (11°–15°N) zonal wind difference averaged in 120°–160°E in global warming run. Values exceeding the 95% (99%) significance level are light (dark) shaded; (b) 51-yr running regression of the surface wind vorticity (m s^{-1}) during JAS(1) upon the NDJ(0) ENSO index.

The increased persistence in both the NWP anticyclone and SST warming over the NIO/SCS are suggestive of an increased feedback between them. The TIO SST influence on the NWP is mediated by the tropospheric Kelvin wave (Xie et al. 2009). Figures 16a and 16b compare tropospheric temperature anomalies in JAS(1) between the twentieth and twenty-second centuries. In both periods, the TIO warming forces a Matsuno–Gill pattern of a Rossby–Kelvin wave couplet. A warm tropospheric Kelvin wave is seen to penetrate into the equatorial western Pacific. The meridional gradient of tropospheric temperature on the northern flank of the Kelvin wave is larger in the twenty-second than twentieth century, consistent with intensified northeasterly wind anomalies at the surface and a strengthened NWP anticyclone. We also compare the NWP SLP between the twentieth and twenty-second century (Figs. 16c,d). The result also shows that NWP anticyclone persists longer in a warmer climate, of which location (120°–160°E) does not change much.

In light of a more persistent warming in TIO SST, it is puzzling that tropospheric temperature correlation over the TIO decreases by 0.1 from the twentieth to twenty-second century. This appears as due to the negative SST anomalies in the equatorial western Pacific in the twenty-second − twentieth-century difference maps (right panels, Fig. 8). The equatorial Pacific cooling excites a Matsuno–Gill pattern of negative sign, reducing the tropospheric warming over the TIO. The contrast between the enhanced TIO warming and a cooler equatorial Pacific in JAS(1), however, strengthens the temperature gradients over the Indo–western Pacific, intensifying surface wind divergence and the surface anticyclone over the subtropical NWP. This is consistent with Terao and Kubota (2005) and Ohba and Ueda (2006), who investigate the effect of such a zonal SST contrast on atmospheric circulation.

The strengthened interaction between NIO SST and the NWP anticyclone may also be facilitated by the mean states change. The tropospheric Kelvin wave–induced Ekman divergence at the surface over the subtropical NWP needs convective feedback to form a pronounced anticyclonic circulation (Xie et al. 2009). Mean convection intensifies from the twentieth to twenty-second century, helping amplifying the NWP anticyclone in response to the equatorial Kelvin wave from the TIO. Changes in mean wind are westerly over the NIO, SCS, and NWP from spring to summer (Fig. 6), expanding the eastward reach of the mean westerlies over the NWP. As a result, NWP SST warming reaches farther eastward in the twenty-second than twentieth century (Fig. 5). Mean westerlies are condition for the second warming in NIO and SCS.

f. NIO warming in a mutlimodel ensemble

To examine if the above results are model dependent, we choose another five models in the CMIP3 archive that can realistically simulate the basin warming over Indian Ocean response to ENSO and compare the NIO warming in JAS(1) before and after global warming. Table 1 shows the regressions of JAS(1) NIO SST anomalies upon the ENSO index in six models. In

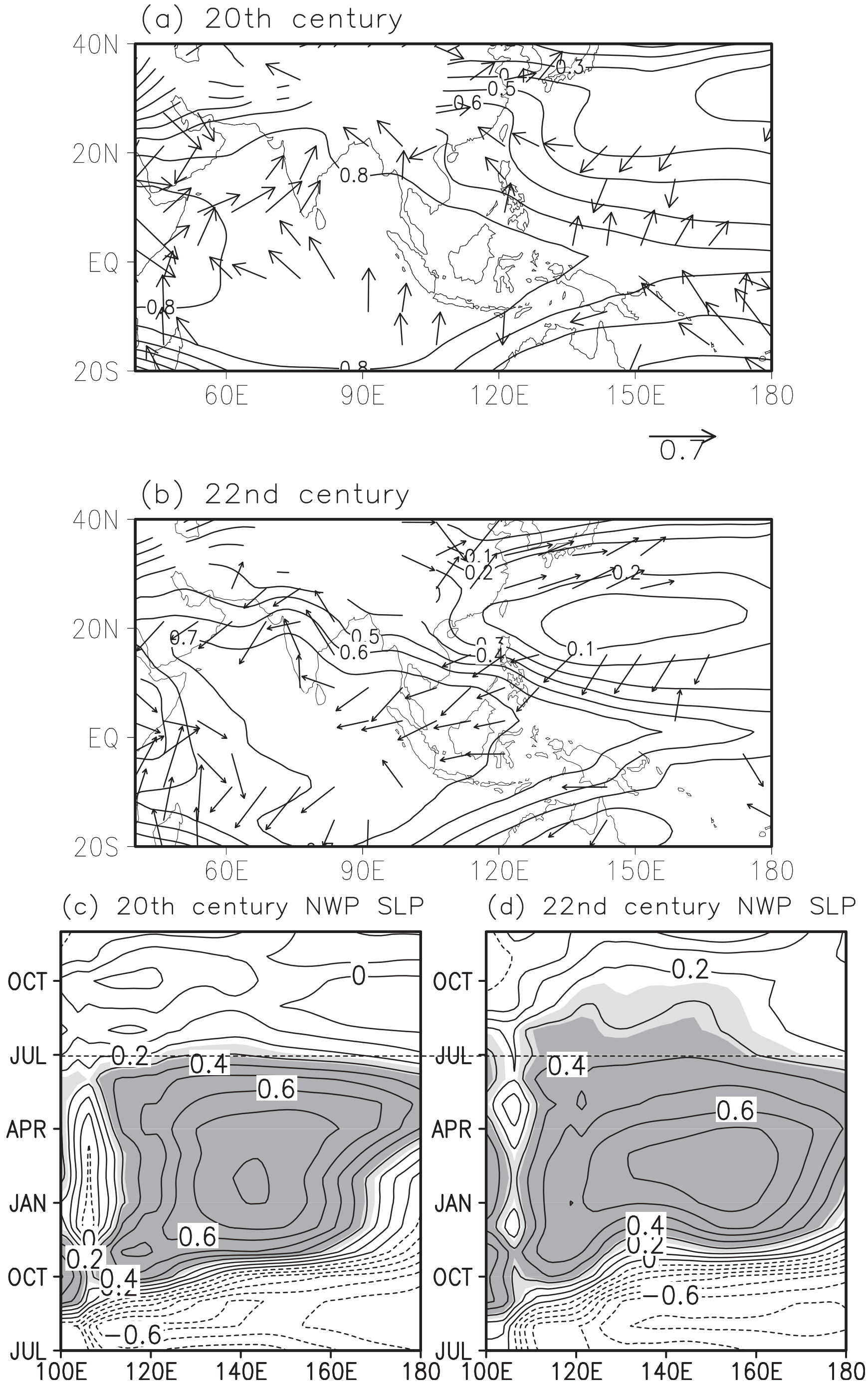

FIG. 16. Correlation with the NDJ(0) ENSO index of tropospheric temperature (contours), and surface wind velocity (vectors) during JAS(1) in (a) twentieth century and (b) twenty-second century. Correlation of SLP average over NWP (12.5°–30°N) upon the ENSO index as a function of longitude and calendar month for (c) the twentieth century and (d) twenty-second century. Values exceeding the 95% (99%) significance level are light (dark) shaded.

summer the NIO warming is enhanced under global warming in all six models, regardless of changes in ENSO amplitude. Further work is underway to investigate the IOB mode simulations by CMIP3 models in detail and will be reported separately. Focusing our analysis on CM2.1 here has enabled us to gain insights into IOB mode changes, which will serve as a useful reference in multimodel studies.

TABLE 1. JAS(1) NIO SST regression on the ENSO index and standard deviations of ENSO index for the twentieth and twenty-second centuries by six CMIP3 models in global warming simulations: regressions exceeding the 95% significance level of a *t* test in bold.

	JAS(1) NIO (°C)		ENSO std dev (°C)	
	Twentieth century	Twenty-second century	Twentieth century	Twenty-second century
GFDL CM2.0	**0.14**	**0.17**	1.13	1.08
GFDL CM2.1	**0.14**	**0.20**	1.37	1.02
CNRM-CM3	**0.15**	**0.16**	1.81	1.63
MRI CGCM2.3.2	0.04	**0.10**	0.81	1.31
UKMO HADCM3	**0.16**	**0.17**	1.02	1.08
UKMO HADGEM1	0.09	**0.15**	0.58	0.86

5. Summary and discussion

We have examined the IOB mode formation following El Niño and its response to global warming using the GFDL coupled model CM2.1. In the unforced control run, the model simulates the delayed warming over the TIO very well; the anticyclonic wind curls in the mature phase of El Niño excite downwelling Rossby waves in the SIO, leading to warm SST anomalies over the SWIO through boreal summer. This SWIO warming is associated with an antisymmetric rainfall/wind pattern that induces the second warming over the NIO after the summer monsoon onset. The second NIO warming excites a warm tropospheric Kelvin wave that anchors an anomalous anticyclonic circulation over the NWP, thereby influencing East Asian climate.

In global warming, ENSO activity is reduced in this model. The IOB mode response to El Niño is nevertheless enhanced in summer, as measured by TIO SST regression upon the ENSO index. The SWIO warming is delayed by about 2 months, accompanied by weakened oceanic Rossby waves and thermocline feedback in the southern TIO. Over the TIO for MAM(1), the meridional SST gradient strengthens, and so does the antisymmetric pattern of rainfall and wind anomalies. These changes in SST, rainfall, and wind are consistent with enhanced WES feedback. The antisymmetric wind pattern that develops in MAM(1) is instrumental in the second warming over NIO/SCS during the following summer, with anomalous northeasterlies opposing the southwest monsoon. The NIO warming persists two months longer in global warming, through JAS(1) in the twenty-second century. The NIO/SCS warming and the NWP anticyclone are coupled through the easterly wind anomalies during summer and fall. The enhanced persistence of the SST warming and NWP anticyclone is suggestive of a stronger coupling between each other. The more persistent NWP anticyclone is facilitated by a SST decrease over the western equatorial Pacific associated with the faster decay of El Niño in global warming. The change in the western Pacific seems related to a shoaling thermocline in the mean as the Walker circulation slows down in the warmer climate. The interannual cooling over the western Pacific strengthens the SST contrast with the warm TIO, sharpening pressure gradients in space and intensifying the NWP anomalous anticyclone. The enhanced antisymmetric pattern over the TIO and prolonged persistence of the NIO/SCS warming and NWP anticyclone suggest a strengthening in air–sea interaction within the TIO and with the western Pacific. As a result, both the IOB mode and its capacitor effect strengthen in global warming.

Observational and atmospheric model studies show that the ENSO-induced basinwide warming over the TIO persists longer since the 1970s (Xie et al. 2010b; Huang et al. 2010). This change is associated with an intensification of SWIO warming, the antisymmetric rainfall/wind pattern, the second NIO warming, and the NWP anomalous anticyclone. A recent study of TIO variability for 1870–2008 suggests that changes in the IOB mode is part of a low-frequency modulation of ENSO (Chowdary et al. 2011b). Our analysis of the CM2.1 future climate projection suggests that the intensification of the IOB mode and its capacitor effect in summer may partly be due to the ongoing anthropogenic global warming via strengthened air–sea interactions over the TIO and with the NWP. This tendency for an enhanced IOB mode and capacitor effect may strengthen as the global warming effect increases relative to natural low-frequency modulation.

Observational and model studies suggest that the TIO basin warming forces easterly winds over the equatorial Pacific (Annamalai et al. 2005b) and leads to a rapid termination of El Niño and a fast transition to La Niña (Kug and Kang 2006; Kug et al. 2006). Indeed, in the model El Niño decays more rapidly in a warmer climate with the enhanced easterlies in the equatorial Pacific (Figs. 7 and 8). The resultant cooling of the equatorial Pacific can excite an atmospheric response that helps the NWP anticyclone persist longer. Relative contributions from Indian Ocean and Pacific SST anomalies to the increased persistence of the NWP anticyclone need to be investigated in future studies.

Acknowledgments. We would like to acknowledge useful comments from anonymous reviewers. We wish to thank Drs. N. C. Johnson and J. S. Chowdary for helpful discussions. This work is supported by the Natural Science Foundation of China (40830106, 41106010, 40921004), the National Basic Research Program of China (2012CB955603), the Fundamental Research Funds for Central Universities of the Ministry of Education of China (201113026), the 111 Project (B07036), the Changjiang and Qianren Programs, the U.S. National Science Foundation, and the Japan Agency for Marine-Earth Science and Technology.

REFERENCES

Abram, N. J., M. K. Gagan, J. E. Cole, W. S. Hantoro, and M. Mudeless, 2008: Recent intensification of tropical climate variability in the Indian Ocean. *Nat. Geosci.,* **1,** 849–853.

Alexander, M. A., I. Blade, M. Newman, J. R. Lanzante, N.-C. Lau, and J. D. Scott, 2002: The atmospheric bridge: The influence of ENSO teleconnections on air–sea interaction over the global oceans. *J. Climate,* **15,** 2205–2231.

Alory, G., S. Wijffels, and G. Meyers, 2007: Observed temperature trends in the Indian Ocean over 1960-1999 and associated mechanisms. *Geophys. Res. Lett.,* **34,** L02606, doi:10.1029/2006GL028044.

An, S.-I., J.-S. Kug, Y.-G. Ham, and I.-S. Kang, 2008: Successive modulation of ENSO to the future greenhouse warming. *J. Climate,* **21,** 3–21.

Annamalai, H., P. Liu, and S.-P. Xie, 2005a: Southwest Indian Ocean SST variability: Its local effect and remote influence on Asian monsoons. *J. Climate,* **18,** 4150–4167.

——, S.-P. Xie, J.-P. McCreary, and R. Murtugudde, 2005b: Impact of Indian Ocean sea surface temperature on developing El Niño. *J. Climate,* **18,** 302–319.

Cai, W., A. Sullivan, and T. Cowan, 2009: Climate change contributes to more frequent consecutive positive Indian Ocean Dipole events. *Geophys. Res. Lett.,* **36,** L23704, doi:10.1029/2009GL040163.

Capotondi, A., A. Wittenberg, and S. Masina, 2006: Spatial and temporal structure of tropical Pacific interannual variability in 20th century coupled simulations. *Ocean Modell.,* **15,** 274–298.

Chiang, J. C. H., and A. H. Sobel, 2002: Tropical tropospheric temperature variations caused by ENSO and their influence on the remote tropical climate. *J. Climate,* **15,** 2616–2631.

——, and B. R. Lintner, 2005: Mechanisms of remote tropical surface warming during El Niño. *J. Climate,* **18,** 4130–4149.

Chowdary, J. S., S.-P. Xie, J.-J. Luo, J. Hafner, S. Behera, Y. Masumoto, and T. Yamagata, 2011a: Predictability of Northwest Pacific climate during summer and the role of the tropical Indian Ocean. *Climate Dyn.,* **36,** 607–621, doi:10.1007/s00382-009-0686-5.

——, ——, H. Tokinaga, Y. Okumura, H. Kubota, N. Johnson, and X.-T. Zheng, 2011b: Inter-decadal variations in ENSO teleconnection to the Indo-western Pacific for 1870–2007. *J. Climate,* in press.

Collins, M., 2005: El Niño- or La Niña-like climate change? *Climate Dyn.,* **24,** 89–104.

——, and Coauthors, 2010: The impact of global warming on the tropical Pacific Ocean and El Niño. *Nat. Geosci.,* **3,** 391–397.

Delworth, T. L., and Coauthors, 2006: GFDL's CM2 global coupled climate models. Part I: Formulation and simulation characteristics. *J. Climate,* **19,** 643–674.

Deser, C., A. S. Phillips, and J. W. Hurrell, 2004: Pacific interdecadal climate variability: Linkages between the tropics and the North Pacific during boreal winter since 1900. *J. Climate,* **17,** 3109–3124.

——, M. A. Alexander, S.-P. Xie, and A. S. Phillips, 2010: Sea surface temperature variability: Patterns and mechanisms. *Ann. Rev. Marine Sci.,* **2,** 115–143, doi:10.1146/annurev-marine-120408-151453.

de Szoeke, S. P., S.-P. Xie, T. Miyama, K. J. Richards, and R. J. O. Small, 2007: What maintains the SST front north of the equatorial cold tongue? *J. Climate,* **20,** 2500–2514.

Du, Y., and S.-P. Xie, 2008: Role of atmospheric adjustments in the tropical Indian Ocean warming during the 20th century in climate models. *Geophys. Res. Lett.,* **35,** L08712, doi:10.1029/2008GL033631.

——, L. Yang, and S.-P. Xie, 2011: Tropical Indian Ocean influence on Northwest Pacific tropical cyclones in summer following strong El Niño. *J. Climate,* **24,** 315–322.

——, S.-P. Xie, G. Huang, and K. Hu, 2009: Role of air–sea interaction in the long persistence of El Niño–induced North Indian Ocean warming. *J. Climate,* **22,** 2023–2038.

Dunn, O. J., and V. A. Clark, 1969: Correlation coefficients measured on the same individuals. *J. Amer. Stat. Assoc.,* **64,** 366–377.

Fedorov, A. V., and S. G. Philander, 2000: Is El Niño changing? *Science,* **288,** 1997–2002.

GFDL Global Atmospheric Model Development Team, 2004: The new GFDL global atmosphere and land model AM2-LM2: Evaluation with prescribed SST simulations. *J. Climate,* **17,** 4641–4673.

Gill, A. E., 1980: Some simple solutions for heat-induced tropical circulation. *Quart. J. Roy. Meteor. Soc.,* **106,** 447–462.

Gordon, C., C. Cooper, C. A. Senior, H. T. Banks, J. M. Gregory, T. C. Johns, J. F. B. Mitchell, and R. A. Wood, 2000: The simulation of SST, sea ice extents and ocean heat transports in a version of the Hadley Centre coupled model without flux adjustments. *Climate Dyn.,* **16,** 147–168.

Griffies, S., M. J. Harrison, R. C. Pacanowski, and A. Rosati, 2003: A technical guide to MOM4. NOAA/Geophysical Fluid Dynamics Laboratory Ocean Group Tech. Rep. 5, 295 pp.

Guilyardi, E., A. Wittenberg, A. Fedorov, M. Collins, C. Wang, A. Capotondi, G. J. van Oldenborgh, and T. Stockdele, 2009: Understanding El Niño in ocean–atmosphere general circulation models: Progress and challenges. *Bull. Amer. Meteor. Soc.,* **90,** 325–340.

Han, W., and Coauthors, 2010: Patterns of Indian Ocean sea level change in a warming climate. *Nat. Geosci.,* **3,** 546–550.

Held, I. M., and B. J. Soden, 2006: Robust responses of the hydrological cycle to global warming. *J. Climate,* **19,** 5686–5699.

Huang, B. H., and J. L. Kinter, 2002: Interannual variability in the tropical Indian Ocean. *J. Geophys. Res.,* **107,** 3319, doi:10.1029/2001JC001278.

Huang, G., K. Hu, and S.-P. Xie, 2010: Strengthening of tropical Indian Ocean teleconnection to the Northwest Pacific since the mid-1970s: An atmospheric GCM study. *J. Climate,* **23,** 5294–5304.

Izumo, T., C. B. Montegut, J.-J. Luo, S. K. Behera, S. Masson, and T. Yamagata, 2008: The role of the western Arabian Sea upwelling in Indian monsoon rainfall variability. *J. Climate,* **21,** 5603–5623.

Johns, T. C., and Coauthors, 2006: The new Hadley Centre climate model HadGEM1: Evaluation of coupled simulations. *J. Climate,* **19,** 1327–1353.

Johnson, N. C., and S.-P. Xie, 2010: Changes in the sea surface temperature threshold for tropical convection. *Nat. Geosci.,* **3,** 842–845.

Kalnay, E., and Coauthors, 1996: The NCEP/NCAR 40-Year Reanalysis Project. *Bull. Amer. Meteor. Soc.,* **77,** 437–471.

Kawamura, R., T. Matsumura, and S. Iizuka, 2001: Role of equatorially asymmetric sea surface temperature anomalies in the Indian Ocean in the Asian summer monsoon and El Niño–Southern Oscillation coupling. *J. Geophys. Res.,* **106,** 4681–4693.

Klein, S. A., B. J. Soden, and N.-C. Lau, 1999: Remote sea surface temperature variations during ENSO: Evidence for a tropical atmospheric bridge. *J. Climate,* **12,** 917–932.

Knutson, T. R., S. Manabe, and D. Gu, 1997: Simulated ENSO in a global coupled ocean–atmosphere model: Multidecadal amplitude modulation and CO_2 sensitivity. *J. Climate,* **10,** 138–161.

Kug, J.-S., and I.-S. Kang, 2006: Interactive feedback between ENSO and the Indian Ocean. *J. Climate,* **19,** 1784–1801.

——, B. P. Kirtman, and I.-S. Kang, 2006: Interactive feedback between ENSO and the Indian Ocean in an interactive ensemble coupled model. *J. Climate,* **19,** 6371–6381.

Lau, N.-C., and M. J. Nath, 2003: Atmosphere–ocean variations in the Indo-Pacific sector during ENSO episodes. *J. Climate,* **16,** 3–20.

Li, S. L., J. Lu, G. Huang, and K. M. Hu, 2008: Tropical Indian Ocean basin warming and East Asian summer monsoon: A multiple AGCM study. *J. Climate,* **21,** 6080–6088.

Lin, S.-J., 2004: A ''vertically Lagrangian'' finite-volume dynamical core for global models. *Mon. Wea. Rev.,* **132,** 2293–2307.

Masumoto, Y., and G. Meyers, 1998: Forced Rossby waves in the southern tropical Indian Ocean. *J. Geophys. Res.,* **103,** 27 589–27 602.

Matsuno, T., 1966: Quasi-geostrophic motions in the equatorial area. *J. Meteor. Soc. Japan,* **44,** 25–43.

Meehl, G. A., G. W. Branstator, and W. M. Washington, 1993: Tropical Pacific interannual variability and CO_2 climate change. *J. Climate,* **6,** 42–63.

Ohba, M., and H. Ueda, 2006: A role of zonal gradient of SST between the Indian Ocean and the western Pacific in localized convection around the Philippines. *SOLA,* **2,** 176–179.

Rao, S. A., and S. K. Behera, 2005: Subsurface influence on SST in the tropical Indian Ocean: Structure and interannual variability. *Dyn. Atmos. Oceans,* **39,** 103–125.

Rayner, N. A., P. Brohan, D. E. Parker, C. K. Folland, J. J. Kennedy, M. Vanicek, T. Ansell, and S. F. B. Tett, 2006: Improved analyses of changes and uncertainties in surface temperature measured in situ since the mid-nineteenth century: The HadSST2 dataset. *J. Climate,* **19,** 446–469.

Saji, N. H., S.-P. Xie, and T. Yamagata, 2006: Tropical Indian Ocean variability in the IPCC 20th-century climate simulations. *J. Climate,* **19,** 4397–4417.

Salas-Mélia, D., and Coauthors, 2005: Description and validation of the CNRM-CM3 global coupled model, CNRM Working Note 103, 36 pp.

Schott, F. A., S.-P. Xie, and J. P. McCreary, 2009: Indian Ocean circulation and climate variability. *Rev. Geophys.,* **47,** RG1002, doi:10.1029/2007RG000245.

Song, Q. N., G. A. Vecchi, and A. Rosati, 2007: Indian Ocean variability in the GFDL CM2 coupled climate model. *J. Climate,* **20,** 2895–2916.

Terao, T., and T. Kubota, 2005: East–west SST contrast over the tropical oceans and the post El Niño western North Pacific summer monsoon. *Geophys. Res. Lett.,* **32,** L15706, doi:10.1029/2005GL023010.

Timmermann, A., J. Oberhuber, A. Bacher, M. Esch, M. Latif, and E. Roeckner, 1999: Increased El Niño frequency in a climate model forced by future greenhouse warming. *Nature,* **398,** 694–697.

van Oldenborgh, G. J., S. Philip, and M. Collins, 2005: El Niño in a changing climate: A multi-model study. *Ocean Sci.,* **1,** 81–85.

Vecchi, G. A., and B. J. Soden, 2007: Global warming and the weakening of the tropical circulation. *J. Climate,* **20,** 4316–4340.

——, ——, A. T. Wittenberg, I. M. Held, A. Leetmaa, and M. J. Harrison, 2006: Weakening of tropical Pacific atmospheric circulation due to anthropogenic forcing. *Nature,* **441,** 73–76.

Wang, B., R. Wu, and T. Li, 2003: Atmosphere–warm ocean interaction and its impact on Asian–Australian monsoon variability. *J. Climate,* **16,** 1195–1211.

Wittenberg, A. T., 2009: Are historical records sufficient to constrain ENSO simulations? *Geophys. Res. Lett.,* **36,** L12702, doi:10.1029/2009GL038710.

——, A. Rosati, N.-C. Lau, and J. J. Ploshay, 2006: GFDL's CM2 global coupled climate models. Part III: Tropical Pacific climate and ENSO. *J. Climate,* **19,** 698–722.

Wu, R., and S.-W. Yeh, 2010: A further study of the tropical Indian Ocean asymmetric mode in boreal spring. *J. Geophys. Res.,* **115,** D08101, doi:10.1029/2009JD012999.

——, B. P. Kirtman, and V. Krishnamurthy, 2008: An asymmetric mode of tropical Indian Ocean rainfall variability in boreal spring. *J. Geophys. Res.,* **113,** D05104, doi:10.1029/2007JD009316.

Xie, P., and P. A. Arkin, 1996: Analyses of global monthly precipitation using gauge observations, satellite estimates, and numerical model predictions. *J. Climate,* **9,** 840–858.

Xie, S.-P., and S. G. H. Philander, 1994: A coupled ocean-atmosphere model of relevance to the ITCZ in the eastern Pacific. *Tellus,* **46A,** 340–350.

——, H. Annamalai, F. A. Schott, and J. P. McCreary, 2002: Structure and mechanisms of South Indian Ocean climate variability. *J. Climate,* **15,** 864–878.

——, K. Hu, J. Hafner, H. Tokinaga, Y. Du, G. Huang, and T. Sampe, 2009: Indian Ocean capacitor effect on Indo-western Pacific climate during the summer following El Niño. *J. Climate,* **22,** 730–747.

——, C. Deser, G. A. Vecchi, J. Ma, H. Teng, and A. T. Wittenberg, 2010a: Global warming pattern formation: Sea surface temperature and rainfall. *J. Climate,* **23,** 966–986.

——, Y. Du, G. Huang, X.-T. Zheng, H. Tokinaga, K. Hu, and Q. Liu, 2010b: Decadal shift in El Niño influences on Indo-western Pacific and East Asian climate in the 1970s. *J. Climate,* **23,** 3352–3368.

Yang, J., Q. Liu, S.-P. Xie, Z. Liu, and L. Wu, 2007: Impact of the Indian Ocean SST basin mode on the Asian summer monsoon. *Geophys. Res. Lett.,* **34,** L02708, doi:10.1029/2006GL028571.

Yu, W., B. Xiang, L. Liu, and N. Liu, 2005: Understanding the origins of interannual thermocline variations in the tropical Indian Ocean. *Geophys. Res. Lett.,* **32,** L24706, doi:10.1029/2005GL024327.

Yukimoto, S., and Coauthors, 2001: The New Meteorological Research Institute coupled GCM (MRI–CGCM2)—Model climate and variability. *Pap. Meteor. Geophys.,* **51,** 47–88.

Yulaeva, E., and J. M. Wallace, 1994: The signature of ENSO in global temperature and precipitation fields derived from the microwave sounding unit. *J. Climate,* **7,** 1719–1736.

Zheng, X.-T., S.-P. Xie, G. A. Vecchi, Q. Liu, and J. Hafner, 2010: Indian Ocean dipole response to global warming: Analysis of ocean–atmospheric feedbacks in a coupled model. *J. Climate,* **23,** 1240–1253.